

Analysis of elasmoid fish imbricated layered scale-tissue systems and their bio-inspired analogues at finite strains and bending[†]

STEPHAN RUDYKH*

Department of Mechanical Engineering, Massachusetts Institute of Technology, Cambridge, MA 02139-4307, USA

*Corresponding author: rudykh@mit.edu

AND

MARY C. BOYCE

School of Engineering and Applied Science, Columbia University, New York, NY 10025, USA

[Received on 10 November 2013; accepted on 14 February 2014]

We examine deformation mechanisms and performance of multilayered structures inspired by imbricated scale-tissue systems of elasmoid fish. Exact analytical solutions are derived for these soft composite structures undergoing finite deformation in compressive and bending loading conditions. The layered structure leads to dramatic coupled shear-compressive deformations which afford distinct and advantageous behaviours in compression and bending. The existence of super-flexible behaviours is found for particular structural configurations. The influence of the geometrical parameters on the composite performance is rigorously analysed.

Keywords: layers; composites; bio-inspired materials; biomimetic; fish scale.

1. Introduction

Design of protective materials and structures has been of long-standing interest for engineers and scientists. When materials are designed to protect mobile units, it is desirable to reduce the weight of the materials. In the case of personal body armour, a certain level of flexibility is needed, especially for joint areas, where various large movements are common. These factors make lightweight polymer-based composites extremely attractive for designing flexible armour. Inspired by natural materials (Bruet *et al.*, 2008), we focus on the mechanical performance of scale-tissue protective systems present in elasmoid fish. These imbricated stiff-scale-soft-tissue systems (see Fig. 1(a–c)) provide an excellent combination of flexibility and protective properties (Meyers *et al.*, 2012; Browning *et al.*, 2013; Yang *et al.*, 2013; Zhu *et al.*, 2013 and references therein). These works study the mechanics of a limited set of systems and loadings. Meyers *et al.* (2012) explored the microstructure of *Arapaimas* scale and performed penetration tests. Browning *et al.* (2013) investigated experimentally and numerically the performance of the composites under compression. Browning *et al.* (2013) also employed the finite element method to study the mechanics of indentation in the composites. Zhu *et al.* (2012, 2013) focused on puncture resistance of scaled skin from striped bass (*Morone saxatilis*).

[†]Dedicated to Professor Ray W. Ogden on the occasion of his 70th birthday

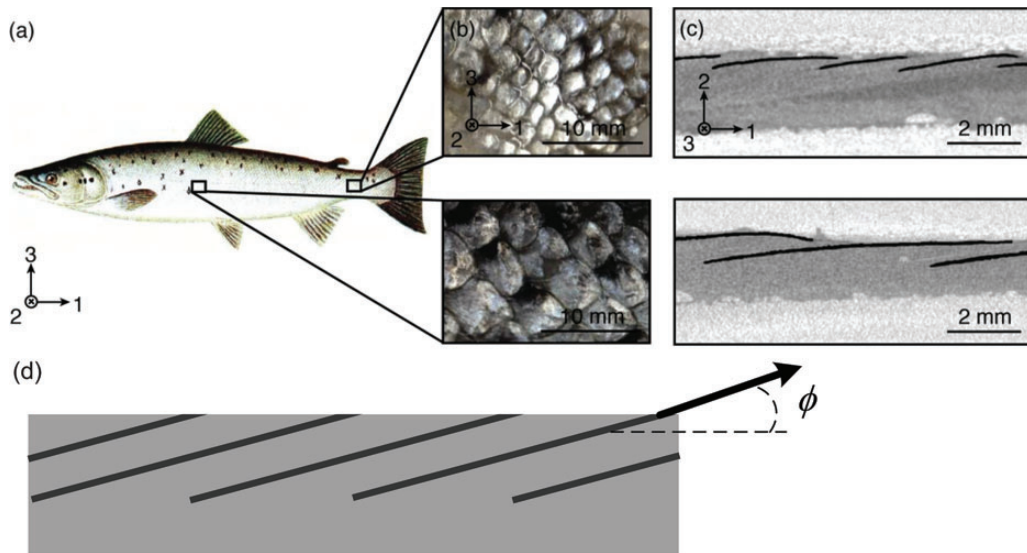


FIG. 1. Elasmoid fish scale assemblies. (a) Atlantic salmon (*Salmo salar*) image (Östman, Elisabeth, Idunskokbok, 1911), (b) overlapping scales and underlying tissue (Browning *et al.*, 2013), (c) micro-computed tomography (μ CT by methods reported by Song *et al.*, 2010; Connors *et al.*, 2012) of structure (false colouring) (Browning *et al.*, 2013). (d) Schematics of scales embedded in a dermal tissue.

Here we present a rigorous analytical model that accounts for large deformation of these soft layered composites in compression and bending loading conditions. The analytical model identifies advantageous configurations and can be used for design and further optimization of the materials. In particular, we approximate composite as a multilayered structure and parametrize the geometry as shown in Fig. 1(d). The derived analytical solutions reveal the existence of super-flexible configurations of the composites subjected to finite bending. These configurations are governed by the inclination angle of the scales, and the response of the materials can be tailored for the required performance. We rigorously analyse the dependence of the material performance on the geometrical parameters. The solution for the applied compressive loads predicts strong coupling between the compressive load and shear modes of deformation. This prediction agrees with the numerical and experimental observations of this mechanism of stress accommodation in the scale-matrix system (Browning *et al.*, 2013). This coupling mechanism enables protection combined with flexibility. Moreover, the mechanism can find its way to applications beyond flexible protective systems, to the fields of robotics and actuators.

The paper is structured as follows. In Section 2, we briefly provide the theoretical background for the non-linear finite elastic deformations. Section 3 is devoted to derivation of an exact analytical solution for the bio-inspired multilayered structures and analysis of the structure response to the compressive loadings. Section 4 provides an analytical solution for the structure subjected to finite bending. Some illustrative examples of stress distribution and bending energy as a function of the microstructure parameters are provided in Section 4. This is followed by concluding remarks.

2. Theoretical background

The Cartesian position vector of a material point in a reference configuration of a body \mathcal{B}_0 is \mathbf{X} , and its position vector in the deformed configuration \mathcal{B} is \mathbf{x} . The deformation of the body is characterized

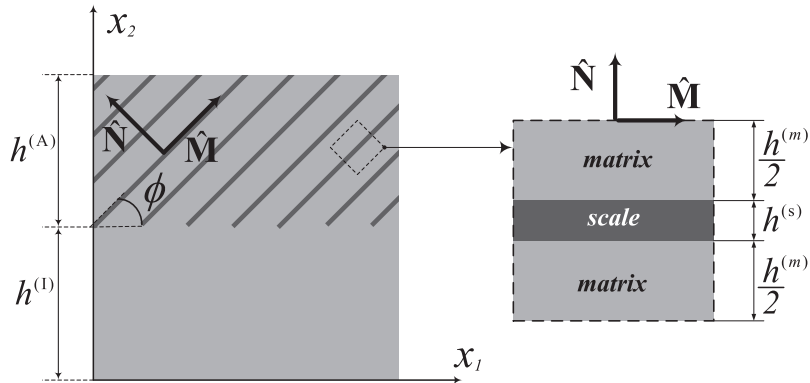


FIG. 2. Schematic of the multilayered material.

by the mapping $\mathbf{x} = \boldsymbol{\chi}(\mathbf{X})$. The deformation gradient is $\mathbf{F} = \partial \boldsymbol{\chi}(\mathbf{X}) / \partial \mathbf{X}$. $J = \det \mathbf{F}$ is the volume ratio. In the absence of body forces, the equilibrium equation is

$$\text{Div } \mathbf{P} = 0, \quad (1)$$

where \mathbf{P} is the nominal stress tensor. The corresponding true or Cauchy stress tensor is related to the nominal stress tensor via the relation $\boldsymbol{\sigma} = J^{-1} \mathbf{P} \mathbf{F}^T$. The differential operator $\text{Div}(\bullet)$ corresponds to the divergency operator in the reference configuration.

Consider hyperelastic materials whose behaviours are characterized by a scalar-valued energy-density function $\Psi(\mathbf{F})$ such that

$$\mathbf{P} = \frac{\partial \Psi(\mathbf{F})}{\partial \mathbf{F}}. \quad (2)$$

For an incompressible material, the nominal stress tensor is

$$\mathbf{P} = \frac{\partial \Psi(\mathbf{F})}{\partial \mathbf{F}} - p \mathbf{F}^{-T}, \quad (3)$$

where p is a pressure-like Lagrange multiplier (Ogden, 1997).

3. Multilayered composites at finite strains

Consider composite materials with multilayered microstructures as seen in Fig. 2.

Assume that the characteristic thickness of the layers in the upper anisotropic layer is significantly smaller than the characteristic size of the upper and lower layers. Such scale separation allows consideration of the upper layer as an effective anisotropic homogeneous material. While the response of the isotropic lower layer is known, the behaviour of the anisotropic upper layer needs to be determined. Under the assumption of scale separation in the layered material, the upper layer is essentially a layered material itself, consisting of alternating stiff–soft layers with homogeneous fields within each phase.

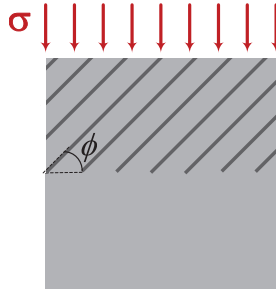


FIG. 3. Schematic of compressive loading of the layered material.

Thus, the mean deformation gradient in the anisotropic layer can be defined as

$$\bar{\mathbf{F}} = c^{(m)} \mathbf{F}^{(m)} + c^{(i)} \mathbf{F}^{(i)}. \quad (4)$$

The deformation gradient in each phase can be obtained by making use of the displacement continuity condition across the interface (i.e. $\mathbf{F}^{(m)} \hat{\mathbf{M}} = \mathbf{F}^{(i)} \hat{\mathbf{M}}$) as (see deBotton, 2005 for details)

$$\mathbf{F}^{(m)} = \bar{\mathbf{F}}(\mathbf{I} + c^{(i)} \alpha \hat{\mathbf{M}} \otimes \hat{\mathbf{N}}) \quad \text{and} \quad \mathbf{F}^{(i)} = \bar{\mathbf{F}}(\mathbf{I} - c^{(m)} \alpha \hat{\mathbf{M}} \otimes \hat{\mathbf{N}}), \quad (5)$$

where the scalar α is obtained from the traction continuity condition

$$[[\boldsymbol{\sigma}]] \cdot \mathbf{n} = \mathbf{0}, \quad (6)$$

where $\mathbf{n} = J\mathbf{F}^{-\top} \hat{\mathbf{N}}$ is normal to the boundary at the current configuration. The notation $[[\bullet]] \equiv (\bullet)^+ - (\bullet)^-$ denotes the jump between the fields in the material across the interface. Furthermore, the total energy-density function of the composite can be expressed as the weighted sum of phase energy-density functions, namely,

$$\tilde{\Psi}^{(A)}(\bar{\mathbf{F}}) = \sum_{r=m,i} c^{(r)} \Psi^{(r)}(\bar{\mathbf{F}}). \quad (7)$$

If the behaviour of the phases can be characterized using neo-Hookean models, then the effective energy-density function of the anisotropic upper layer can be obtained from Equations (7) and (5), where

$$\alpha = \frac{\mu^{(i)} - \mu^{(m)}}{c^{(m)} \mu^{(i)} + c^{(i)} \mu^{(m)}} \frac{\bar{\mathbf{F}} \hat{\mathbf{N}} \cdot \bar{\mathbf{F}} \hat{\mathbf{M}}}{\bar{\mathbf{F}} \hat{\mathbf{M}} \cdot \bar{\mathbf{F}} \hat{\mathbf{M}}}. \quad (8)$$

Once the homogenized energy-density function for the upper layer is obtained, the boundary value problem of the macroscopic sandwich problem can be solved by repeating a similar procedure, such that the total energy-density function of the structure is

$$\Psi^{(\text{total})}(\bar{\mathbf{F}}) = c^{(A)} \tilde{\Psi}^{(A)}(\bar{\mathbf{F}}) + c^{(I)} \tilde{\Psi}^{(I)}(\bar{\mathbf{F}}). \quad (9)$$

Note that it is mathematically convenient to assume that both phases can be characterized by a neo-Hookean model. The presented further results are based on this assumption.

Loading Conditions. Consider the response of the composite subjected to compressive traction load, as shown in Fig. 3. The macroscopic traction boundary condition at $X_2 = h^{(I)}$ and $X_2 = h^{(I)} + h^{(A)}$ is

such that only $\sigma_{22} = -\sigma$ has non-zero value. Owing to the anisotropy, the compressive load can result, in general, in both shear and compressive deformation modes within the anisotropic layer. Therefore, the corresponding macroscopic deformation gradient is assumed to be

$$\bar{\mathbf{F}} = \lambda^{-1} \mathbf{e}_1 \otimes \mathbf{e}_1 + \lambda \mathbf{e}_2 \otimes \mathbf{e}_2 - \gamma \mathbf{e}_1 \otimes \mathbf{e}_2 + \mathbf{e}_3 \otimes \mathbf{e}_3. \quad (10)$$

The amount of shear γ can be obtained together with λ from the corresponding boundary conditions. In particular, the following system of equations:

$$\begin{cases} \sigma_{11} - \sigma_{22} = f_1(\lambda, \gamma) = \sigma, \\ \sigma_{12} = f_2(\lambda, \gamma) = 0 \end{cases} \quad (11)$$

can be solved for λ and γ . Practically, the problem can be more effectively solved by setting the unknowns to be γ and σ while assuming λ to be an independent variable. Thus, the corresponding value of the amount of shear $\gamma(\lambda)$ is obtained from solving (11)-2. Next, the specific stress component $\sigma = \sigma(\lambda)$ is calculated directly from (11)-1, since $\gamma(\lambda)$ is known. Note that in this case we need to consider only the behaviour of the upper anisotropic layer, since the deformation and stresses that develop in the lower homogeneous layer are simply given by $\sigma_{11} - \sigma_{22} = \mu^{(m)}(\lambda^2 - \lambda^{-2})$. Obviously, there is no shear deformation in the lower homogeneous layer. Thus, the total mean compressive stress in the structure is the weighted sum of the stresses in the upper and lower layers. Consequently, we focus here on the determination of the stresses and the shear mode of deformation in the upper anisotropic layer. In this work, we present results for the situation when the soft matrix and the stiff inclusion plates are characterized by a significant contrast in their shear moduli; in particular, we fix $\mu^{(i)}/\mu^{(m)} = 1160$ (this ratio can be achieved in modern multimaterial multiphase 3D printing techniques [Li et al., 2013](#)). We also normalize the resulting quantities, such as stress and stored energy, by $\mu^{(m)}$ where possible.

Figure 4 shows the dependence of the amount of shear strain, γ , in the anisotropic layer on the lamination angle for composites subjected to different levels of compression from a compression ratio of $\lambda = 0.99$ to 0.8. Volume fractions of the stiffer layers are $c^{(i)} = 0.05$ (a), 0.1 (b), 0.15 (c) and 0.2 (d). The amount of shear during compression increases rapidly with an increase of the lamination angle from 0 until a prominent peak at $\phi \simeq 4^\circ$. This is followed by a decrease in the amount of shear. The shear function decreases monotonically and, at some lamination angle past $\phi = 45^\circ$, the amount of shear changes sign and becomes negative. The magnitude of the negative shear reaches a local maximum at $\phi = 90^\circ$. However, it is important to note that, at this point, the function $\gamma(\phi)$ can take one of the three values $\pm\gamma(90^\circ)$ or 0. In the last case, however, larger compressive stress is needed. We also note that, in the vicinity of $\phi = 90^\circ$, the composites may exhibit buckling upon achieving critical compressive load. This phenomenon of elastic instabilities in transversely isotropic composites is well known in the literature (see, for example, [Triantafyllidis and Maker, 1985](#); [Merodio and Ogden, 2002](#); [Nestorovic and Triantafyllidis, 2004](#); [Merodio and Ogden, 2005](#); [Merodio and Neff, 2006](#); [Rudykh and deBotton, 2012](#); [Li et al., 2013](#); [Rudykh and Boyce, 2014b](#)). The bifurcation occurs when a critical compression level in the direction of the plates is reached; however, the shearing mechanism works to decrease the compression in the plates and, hence, to avoid buckling. However, in composites with large lamination angles, the shearing mechanism cannot completely eliminate compression in the plate direction and buckling may occur upon achieving a critical strain ([Rudykh and Boyce, 2014a](#)). The critical strain in these non-aligned-with-loading layered materials can be estimated by combining the exact analytical solution for a primary branch of solution with a bifurcation analysis (for example, [Rudykh and Bertoldi, 2013](#); [Rudykh et al., 2014](#), where the authors provided estimations for onset of bifurcations in

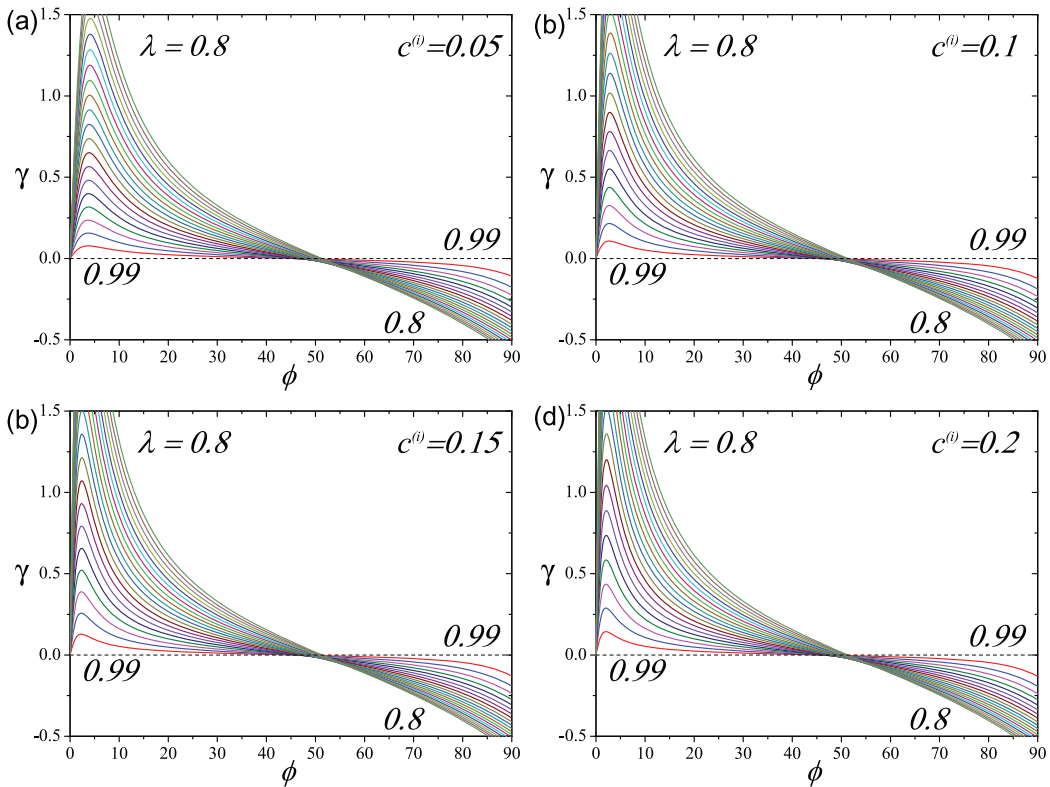


FIG. 4. Dependence of amount of shear on lamination angle. Volume fractions of the stiffer layers are $c^{(i)} = 0.05$ (a), 0.1 (b), 0.15 (c) and 0.2 (d).

non-aligned loaded laminates for the purely mechanical case and for coupled magnetomechanical and electromechanical cases, respectively). The biological systems considered are characterized by small lamination angles, so the protection properties can be maximized. Additionally, the failure mechanism can be a source of a prominent softening in the composite and, consequently, a reduction in the protective properties. In this respect, composites with small lamination angles are more advantageous for protection purposes. For these reasons, we mostly focus on the performance of composites with relatively small lamination angles. The bifurcation phenomenon, indeed, is not observed in the wide range of lamination angles ($\phi \lesssim 45^\circ$), where a compression would cause tension in stiff plates; in that case, the shearing mechanism is opposite and works to minimize the tension in the stiff phase. Once again, for these laminates the bifurcations do not occur. Consequently, the stability analysis is left outside of the scope of this work.

We note that the pronounced shear deformation is a result of the high contrast is the shear modulus ratio chosen. As the ratio is increased, the resulting shear deformation increases; a decrease in the ratio leads to a decrease in the amount of shear and in the case of $\mu^{(i)}/\mu^{(m)} = 1$, the solution reduces to the homogeneous case producing $\gamma = 0$.

At the small lamination angles, even relatively low compressive loadings would lead to a very high extension of the layers if the shear mode of deformation were constrained. Consequently, the material

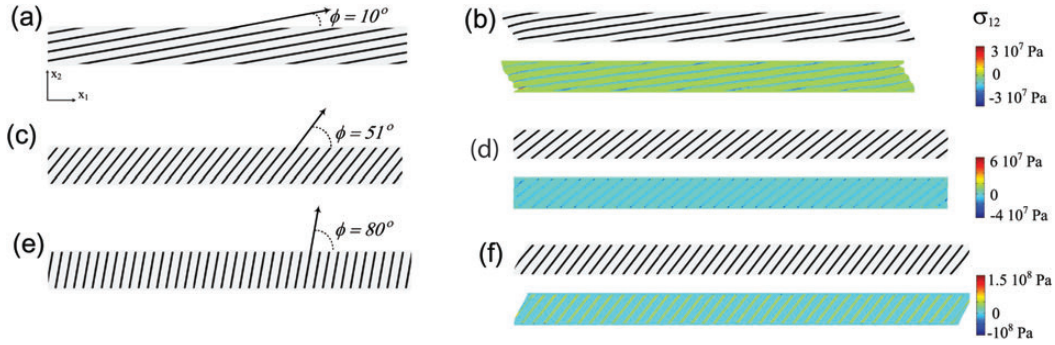


FIG. 5. FE illustration of the micromechanics of the layered materials subjected to compression. The undeformed composites are in the left column: (a) $\phi = 10^\circ$, (c) 51° and (e) 80° . The composites subjected to compression $\lambda = 0.8$ are in the right column: (b) $\phi = 10^\circ$, (d) 51° and (f) 80° . The volume fraction of the stiff plates $c^{(i)} = 0.2$.

reacts by rotating the layers back, and a positive amount of shear γ is generated. With further increase of the lamination angle after the maximum peak, the virtual (if the shear mode were constrained and avoided) tension deformation of the layers decreases gradually with an increase of a lamination angle. This decrease in the virtual tension leads to the reduction of the actual amount of shear. This continues until $\phi \simeq 45^\circ$, where the virtual tension switches to the virtual compression, and at this point no shear mode deformation is generated. Naturally, in the configuration of these compressive virtual deformations, the sign of γ changes, since now the material reacts to compensate for the virtual compression.

Obviously, the deformation regime can switch from tension to compression and vice versa as the compressive load is applied. From the geometric consideration, we obtain that the length of the undeformed plate is $L_0 = h^{(A)} \sqrt{1 + \tan^2 \phi}$, while the length of the deformed plate is $l = h^{(A)} \sqrt{\lambda^2 + \lambda^{-2} \tan^2 \phi}$. Clearly, the plate is compressed when $l < L_0$, and is in tension otherwise. The switch of the deformation regime occurs at $l = L_0$. Excluding the trivial solution of $\lambda = 1$, we obtain the critical stretch ratio at which the switch occurs

$$\lambda = \left(\frac{1 + \cos 2\phi}{1 - \cos 2\phi} \right)^{1/2}. \quad (12)$$

Illustrative examples obtained from finite element simulations are presented in Fig. 5 for composite with $c^{(i)} = 0.2$ and different lamination angles $\phi = 10^\circ$ in (a) and (b), 51° in (c) and (d), and 80° in (e) and (f). The left column is for undeformed microstructure, while the right column represents the microstructures of composites and the shear stress distribution of the composites subjected to compression of $\lambda = 0.8$. The ratio between the stiff plates' thickness and specimen height is ~ 0.045 . As predicted by the analytical model, we observe positive shearing $\gamma > 0$ for small lamination angles ($\phi = 10^\circ$ shown in (a) and (b)); a transition regime is illustrated by (c) and (d) for an intermediate lamination angle $\phi = 51^\circ$, where the coupling between compressive and shear modes of deformation is weak; negative shearing ($\gamma < 0$) is observed for a large lamination angle, $\phi = 80^\circ$.

Next we consider the influence of volume fraction of the constituents. Figure 6 shows the dependence of the amount of shear in the anisotropic layer as a function of volume fraction of the stiffer phase at different levels of compression. The results are presented for composites with $\phi = 5^\circ$ (a), $\phi = 10^\circ$ (b), $\phi = 15^\circ$ (c) and $\phi = 20^\circ$ (d). For all these cases the curves are symmetric with respect to $c^{(i)} = 0.5$. The amount of shear increases rapidly with an initial increase of the volume fraction; then,

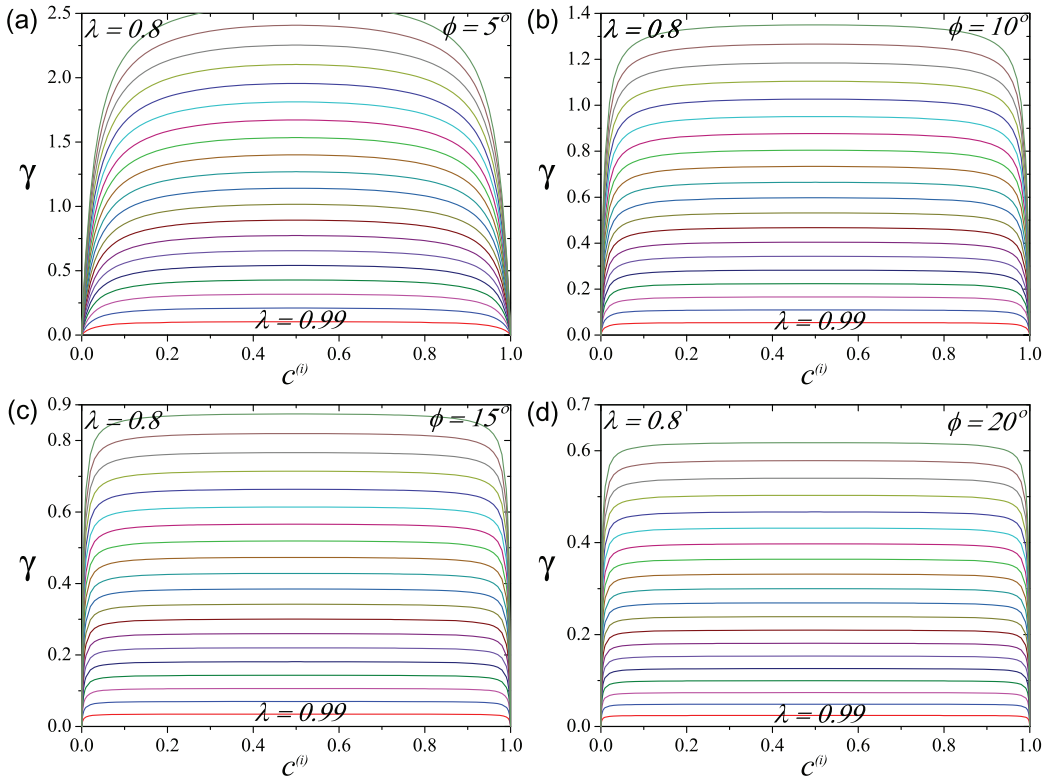


FIG. 6. Dependence of the amount of shear on volume fraction. The lamination angles are $\phi = 5^\circ$ (a), $\phi = 10^\circ$ (b), $\phi = 15^\circ$ (c) and $\phi = 20^\circ$ (d).

however, the slope decreases and the curve flattens until it reaches $c^{(i)} = 0.5$. The change in the slope becomes more prominent for lower compressions (larger λ). Although this behaviour is generic for the lamination angles considered, there are some differences. As the lamination angle increases, the shear deformation decreases. This is in agreement with the previous findings (see Fig. 4). Additionally, we observe that the initial slope increases with an increase in the lamination angle. Moreover, the change in the slope becomes more pronounced, and the point at which the curve changes the behaviour shifts towards $c^{(i)} = 0$ (or, symmetrically, towards $c^{(i)} = 1$). Consequently, for composites with larger lamination angles of the considered range, a change in volume fraction has little effect on the amount of shear in a large range of volume fractions except in the vicinity of $c^{(i)} = 0$ and 1.

Consider next the dependence of stresses on the microstructure parameters. Figure 7 shows the dependence of compressive stress $\tilde{\sigma} = \sigma / \mu^{(m)}$ on the lamination angle at different levels of compression (from $\lambda = 0.99$ to 0.8). The results are presented for composites with $c^{(i)} = 0.05$ (a), 0.1 (b), 0.15 (c) and 0.2 (d). The stress is maximal at $\phi = 0$; it rapidly decreases with an increase in the lamination angle. Then, at some angle, the curves flatten [see, for example, the curve for $\lambda = 0.99$ (red curve in the on-line version) in Fig. 7(a)] and further change in the lamination angles does not influence the stress significantly. However, when the lamination angle approaches high values ($\phi \simeq 70^\circ$ for $\lambda = 0.99$), the stress increases rapidly until it reaches the local maximum at $\phi = 90^\circ$.

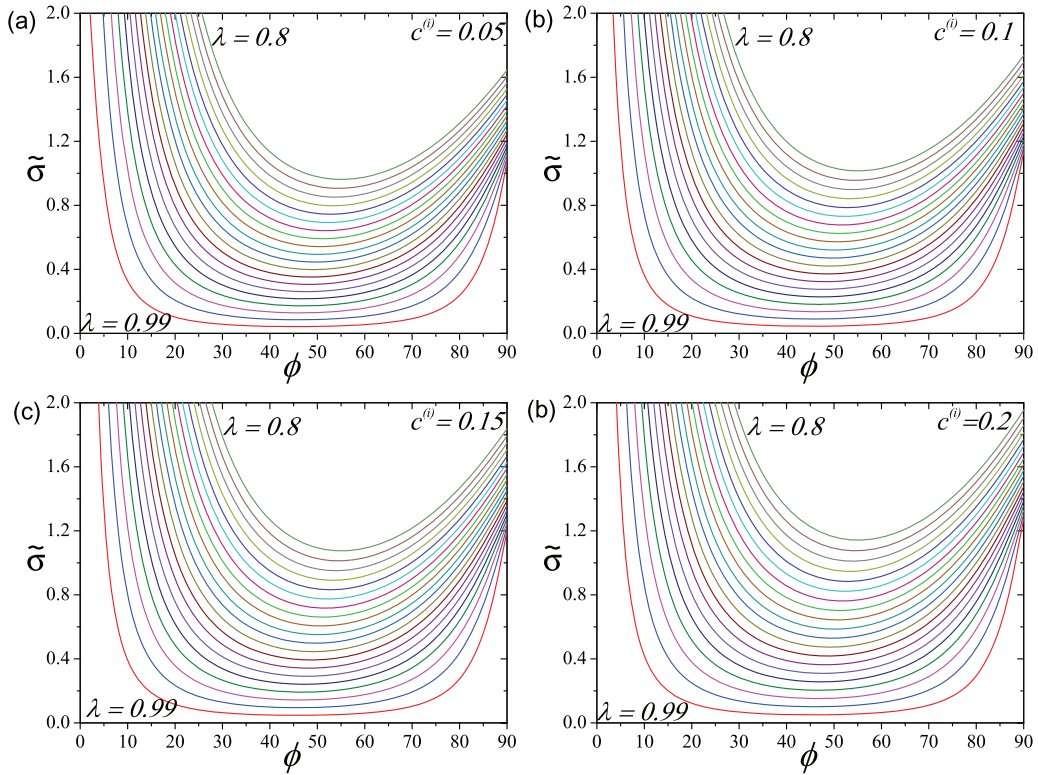


FIG. 7. Dependence of stress on lamination angle. Volume fractions of the stiffer layers are $c^{(i)} = 0.05$ (a), 0.1 (b), 0.15 (c) and 0.2 (d).

As expected from physical grounds, the stress level increases with an increase in compression. This is also accompanied by a gradual change in the curve shape such that the transitions between the decreasing and increasing parts of the curves become smoother, and at high compressive levels (for example, $\lambda = 0.8$) we do not observe the plateau at which the stress scarcely changes with a change in the lamination angle.

We observe a clear similarity between the families of curves for composites with different volume fractions in the considered range $c^{(i)} = 0.05$ (a), 0.1 (b), 0.15 (c) and 0.2 (d), although, as we can conclude from the picture, the stress level increases as the volume fraction is increased.

We investigate the influence of phase volume fraction in detail in Fig. 8, which shows the dependence of the compressive stress as a function of the volume fraction of the stiffer phase for different lamination angles, namely, $\phi = 5^\circ$ (a), $\phi = 10^\circ$ (b), $\phi = 15^\circ$ (c) and $\phi = 20^\circ$ (d).

At low compressive loads [for example, the curve corresponding to $\lambda = 0.99$ (red curve in the on-line version)], we observe the stress-concentration behaviour characterized by initial rapid growth of the stress level. This is followed by a large range of volume fractions, where the stress grows slowly with an increase in volume fraction. However, when the volume fraction becomes large enough, the material locks up and the stress starts to grow rapidly until it reaches the maximum at $c^{(i)} = 1$. The behaviour of the stress-concentration curves alters with an increase of compressive load λ . The range of initial growth widens and the slow-growth range of concentrations shortens. Thus, at some compressive

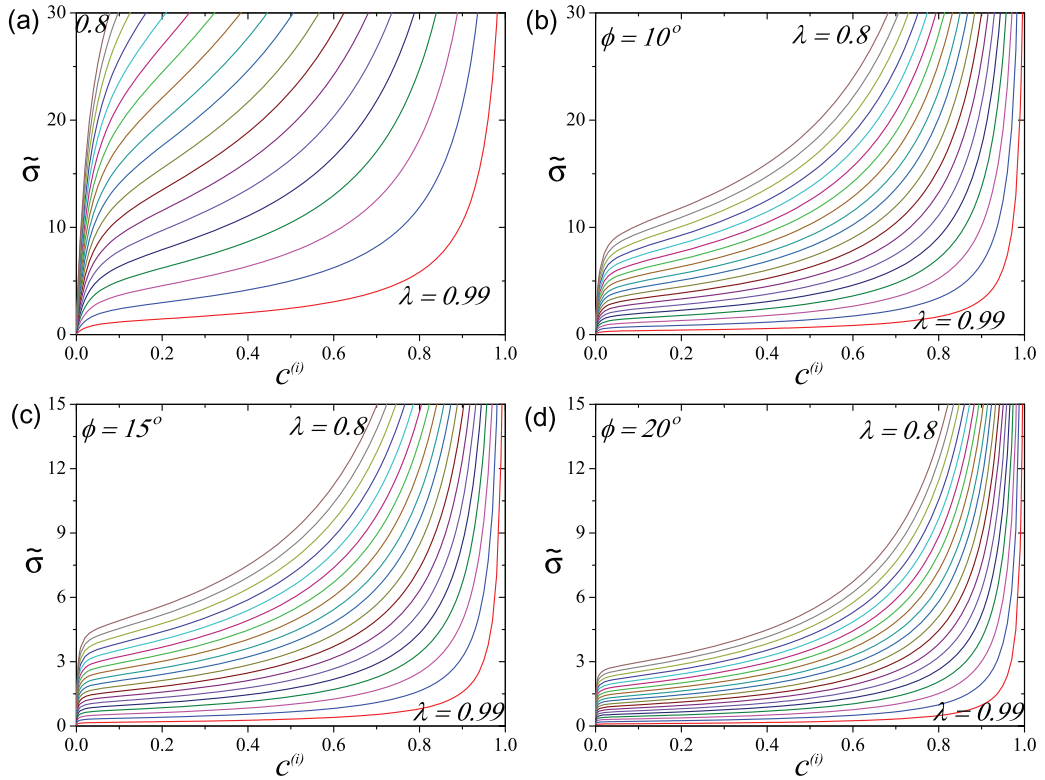


FIG. 8. Dependence of stress on volume fraction. The lamination angles are $\phi = 5^\circ$ (a), $\phi = 10^\circ$ (b), $\phi = 15^\circ$ (c) and $\phi = 20^\circ$ (d).

loads the transition range of volume fractions almost disappears, and we observe a rather abrupt change in the curve slopes. In agreement with the previous findings, we observe that the stress level decreases with an increase in lamination angles, in the range considered in Fig. 8(a–d).

4. Multilayered composites at finite bending

In this section, we consider the multilayered structure subjected to finite bending. First, we revisit the theory of hyperelastic materials at finite bending provided by Rivlin (1949) and recently considered by Destrade *et al.* (2009, 2010), Roccabianca *et al.* (2010), and further extended to layered materials by Roccabianca *et al.* (2011). Then we apply the theory to the more complicated scale-tissue structure, analysing the influence of geometrical parameters on the composite performance at finite bending.

It is convenient to introduce a cylindrical coordinate system for the deformed configuration of the multilayered structure. The schematics of the undeformed and deformed states are depicted in Fig. 9. The length of the specimen in the undeformed state is denoted by l_0 . The thicknesses of the isotropic and anisotropic layers are $h_0^{(1)}$ and $h_0^{(2)}$, respectively; both in the undeformed state. The corresponding thicknesses in the deformed state are denoted by $h^{(1)}$ and $h^{(2)}$. The coordinates of each point in the deformed configuration are defined by functions

$$r = r(x_1), \quad \theta = \theta(x_2) \quad \text{and} \quad z = x_3. \quad (13)$$

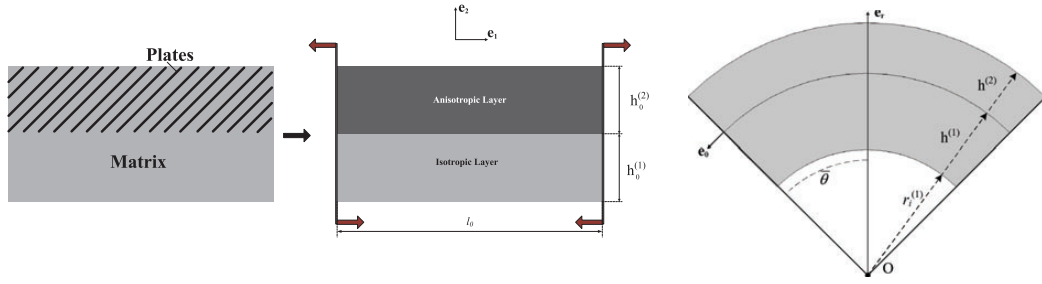


FIG. 9. Schematics of multilayered material subjected to bending.

Thus the deformation gradient is

$$\mathbf{F} = \lambda_r \mathbf{e}_r \otimes \mathbf{e}_1 + \lambda_\theta \mathbf{e}_\theta \otimes \mathbf{e}_2 + \mathbf{e}_3 \otimes \mathbf{e}_3, \quad (14)$$

where $\lambda_r = dr/dx_1$ and $\lambda_\theta = d\theta/dx_2$. Note that due to the plane-strain constraint $\lambda_z = 1$. The deformation is prescribed via the parameter $\bar{\theta}$, which is a half angle segment occupied by the multilayer in the deformed state (see Fig. 9). It can be shown that the principal stretches are

$$\lambda_r = \frac{l_0}{2\bar{\theta}r}, \quad \lambda_\theta = \frac{2\bar{\theta}r}{l_0} \quad \text{and} \quad \lambda_z = 1. \quad (15)$$

Incompressibility implies that, for the anisotropic layer,

$$h^{(2)} = \sqrt{\frac{l_0 h_0^{(2)}}{\bar{\theta}} + r_i^{(2)} - r_i^{(1)}}, \quad (16)$$

where $r_i^{(2)} = r_i^{(1)} + h^{(1)}$ is the inner radius of the anisotropic layer. Similarly, for the isotropic layer, we can write

$$r_i^{(1)} = \frac{l_0 h_0^{(1)}}{2\bar{\theta}h^{(1)}} - \frac{h^{(1)}}{2}. \quad (17)$$

Combining (16) and (17), we have

$$h^{(2)} = -\frac{l_0 h_0^{(1)}}{2\bar{\theta}h^{(1)}} - \frac{h^{(1)}}{2} + \sqrt{\left(\frac{l_0 h_0^{(1)}}{2\bar{\theta}h^{(1)}} + \frac{h^{(1)}}{2}\right)^2 + \frac{l_0 h_0^{(1)}}{\bar{\theta}}}. \quad (18)$$

Clearly, the thickness of the anisotropic layer in the deformed state is a function of $h^{(1)}$, which can be determined from the solution of the boundary value problem.

The equilibrium equations are

$$\frac{\partial \sigma_r^{(s)}}{\partial r} + \frac{\sigma_r^{(s)} - \sigma_\theta^{(s)}}{r} = 0 \quad \text{and} \quad \frac{\partial \sigma_\theta^{(s)}}{\partial \theta} = 0, \quad (19)$$

where $s = 1, 2$ denote the corresponding layer. The stress components are given by

$$\sigma_i = \lambda_i \frac{\partial \Psi(\lambda_i)}{\partial \lambda_i} - p, \quad (20)$$

with $\lambda_r \lambda_\theta = 1$ (Ogden, 2008). Note that there is no summation on repeated indices in (20). Since the stretch depends only on r , (19)₂ is satisfied automatically. Moreover, $(\sigma_\theta - \sigma_r)/r = d\Psi/dr$ because

$$\frac{d\Psi}{dr} = \frac{\partial \Psi}{\partial \lambda_r} \frac{\partial \lambda_r}{\partial r} + \frac{\partial \Psi}{\partial \lambda_\theta} \frac{\partial \lambda_\theta}{\partial r} = -\frac{\partial \Psi}{\partial \lambda_r} \frac{\lambda_r}{r} + \frac{\partial \Psi}{\partial \lambda_\theta} \frac{\lambda_\theta}{r} = \frac{\sigma_\theta - \sigma_r}{r}, \quad (21)$$

where (15) was used. Hence, the equilibrium equation (19) can be written as

$$\frac{d\sigma_r^{(s)}}{dr} = \frac{d\Psi^{(s)}}{dr}, \quad (22)$$

which after integration yields

$$\sigma_r^{(s)} = \hat{\Psi}^{(s)}(\lambda(r)) + A^{(s)}, \quad (23)$$

where $\hat{\Psi} = \Psi(\lambda^{-1}, \lambda, 1)$ with $\lambda = \lambda_\theta$, and $A^{(s)}$ is an unknown integration constant. The interface traction continuity condition reads

$$\sigma_r^{(1)}(r_i^{(1)} + h^{(1)}) = \sigma_r^{(2)}(r_i^{(2)}). \quad (24)$$

The traction-free condition at the external boundaries reads

$$\sigma_r^{(1)}(r_i^{(1)}) = 0 \quad \text{and} \quad \sigma_r^{(2)}(r_i^{(2)} + h^{(2)}) = 0. \quad (25)$$

Equation (25) together with (23) yields

$$A^{(1)} = -\hat{\Psi}^{(1)}(\lambda(r_i^{(1)})) \quad \text{and} \quad A^{(2)} = -\hat{\Psi}^{(2)}(\lambda(r_i^{(2)} + h^{(2)})). \quad (26)$$

Combining (26)₁, (24) and (23), we obtain

$$\hat{\Psi}^{(1)}(\lambda(r_i^{(1)} + h^{(1)})) - \hat{\Psi}^{(1)}(\lambda(r_i^{(1)})) - \hat{\Psi}^{(2)}(\lambda(r_i^{(2)})) = A^{(2)}, \quad (27)$$

and, together with (26)₂,

$$\hat{\Psi}^{(1)}(\lambda(r_i^{(1)} + h^{(1)})) - \hat{\Psi}^{(1)}(\lambda(r_i^{(1)})) - \hat{\Psi}^{(2)}(\lambda(r_i^{(2)})) + \hat{\Psi}^{(2)}(\lambda(r_i^{(2)} + h^{(2)})) = 0. \quad (28)$$

Thus, the unknown parameter $h^{(1)}$ can be calculated from (28) in which $r^2 = r_i^{(1)} + h^{(1)}$, while $r_i^{(1)}$ and $h^{(2)}$ are substituted by the expression given in (17) and (18), respectively.

Once $h^{(1)}$ is determined, the stress distribution can be evaluated. The radial component of stress is obtained by substituting (26) in (23), resulting in

$$\sigma_r^{(1)} = \hat{\Psi}^{(1)}(\lambda(r)) - \hat{\Psi}^{(1)}(\lambda(r_i^{(1)})) \quad (29)$$

and

$$\sigma_r^{(2)} = \hat{\Psi}^{(2)}(\lambda(r)) - \hat{\Psi}^{(2)}(\lambda(r_i^{(2)} + h^{(2)})). \quad (30)$$

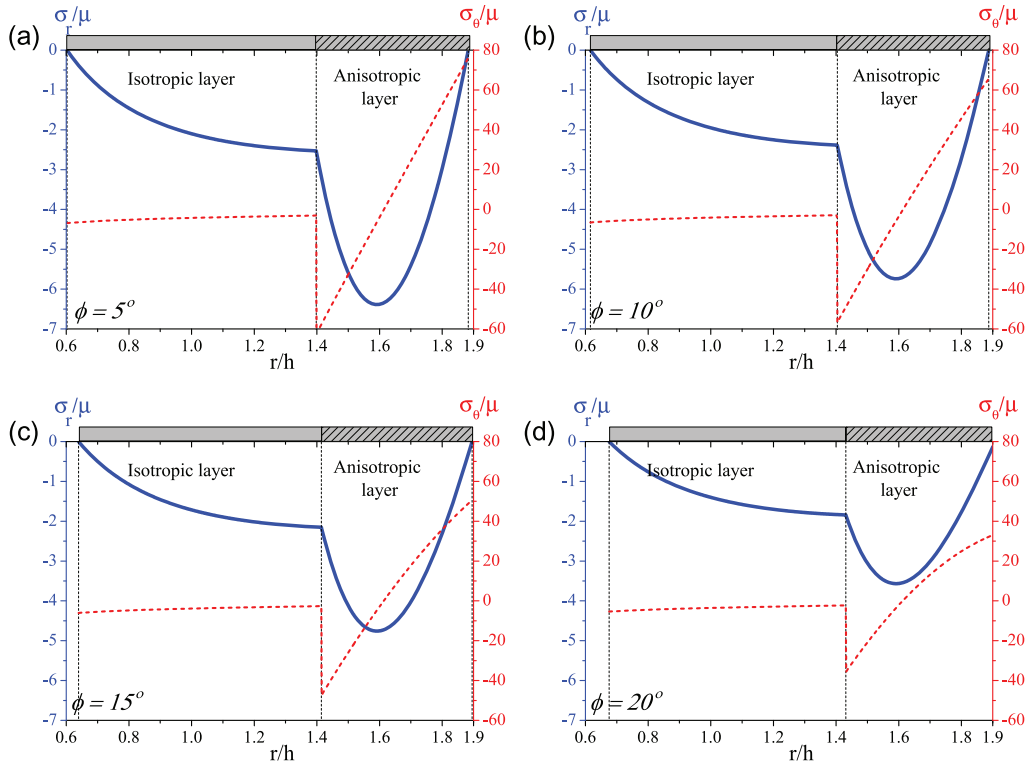


FIG. 10. Stress distributions in the composites subjected to bending $\bar{\theta} = 0.5\pi$. $\phi = 5^\circ$ (a), 10° (b), 15° (c) and 20° (d).

The lateral component is obtained from (19)₁ by using expression (29) and (30) for isotropic and anisotropic layers, respectively, yielding

$$\sigma_\theta^{(1)} = r\hat{\Psi}^{(1)'}(\lambda(r)) + \hat{\Psi}^{(1)}(\lambda(r)) - \hat{\Psi}^{(1)}(\lambda(r_i^{(1)})) \quad (31)$$

and

$$\sigma_\theta^{(2)} = r\hat{\Psi}^{(2)'}(\lambda(r)) + \hat{\Psi}^{(2)}(\lambda(r)) - \hat{\Psi}^{(2)}(\lambda(r_i^{(2)} + h^{(2)})). \quad (32)$$

Finally, the total energy associated with the bending deformation can be calculated as

$$\hat{\Psi}^{\text{total}} = \int_{r_i^{(1)}}^{r_i^{(1)}+h^{(1)}} \hat{\Psi}^{(1)}(\lambda(r))dr + \int_{r_i^{(2)}}^{r_i^{(2)}+h^{(2)}} \hat{\Psi}^{(2)}(\lambda(r))dr. \quad (33)$$

For the homogeneous lower layer, the integration yields

$$\int \hat{\Psi}^{(1)}(\lambda(r))dr = \mu^{(m)} \left(\frac{2\bar{\theta}^2 r^3}{3l_0^2} - \frac{l_0^2}{8\bar{\theta}^2 r} - r \right). \quad (34)$$

Figure 10 shows the distribution of stresses in the isotropic and anisotropic layers. The results are presented for composites with $c^{(i)} = 0.1$ and various lamination angles ($\phi = 5^\circ$ (a), 10° (b), 15° (c)

and 20° (d)) The specimens are of length-to-height ratio $l_0/(h_0^{(1)} + h_0^{(2)}) = 5$, and with equal heights of anisotropic and isotropic layers. The composites are subjected to finite bending of $\bar{\theta} = \pi/2$.

The radial stress, σ_r , normalized by the shear modulus of soft matrix is presented by continuous curves (blue curves in the on-line version), while the normalized azimuthal stress, σ_θ , is denoted by the dashed curves (red dashed curves in the on-line version). Since these components have different magnitudes, we use different axes for presenting the distributions of the stresses. In particular, the values of σ_r are reported at the left axis, while σ_θ is reported at the right axis. The stresses are plotted as functions of the radius r normalized by the total height of the specimen in the undeformed configuration, $h = (h_0^{(1)} + h_0^{(2)})$. The boundary of the layers are marked by thin vertical lines.

The radial component of stress tensor, being negative, increases in its absolute value as we advance from the bottom of the isotropic layer towards the anisotropic layer, according to

$$\sigma_r = \frac{\mu^{(m)}}{2} \left(\frac{l_0^2}{4\bar{\theta}^2} \left(\frac{1}{r^2} - \frac{1}{r_i^{(1)2}} \right) + \frac{4\bar{\theta}^2}{l_0^2} (r^2 - r_i^{(1)2}) \right). \quad (35)$$

At the interface between the isotropic and anisotropic layers, an abrupt change in the stress function occurs. The closed form expression for the stress in the anisotropic upper layer is very long and, therefore, is not included here. We observe a rapid increase of the stress component until it reaches the peak at about $r/h = 1.6$ (depending on the composite), at which point the derivative of the stress function changes the sign, and the absolute value of radial stress starts decreasing. That continues until the value of the radial stress becomes zero at the upper boundary of the anisotropic layer.

The azimuthal stress in the isotropic layer is given by

$$\sigma_\theta = \frac{\mu^{(m)}}{2} \left(\frac{4\bar{\theta}^2}{l_0^2} (3r^2 - r_i^{(1)2}) - \frac{l_0^2}{4\bar{\theta}^2} \left(\frac{1}{r^2} + \frac{1}{r_i^{(1)2}} \right) \right). \quad (36)$$

The stress takes the value

$$\sigma_\theta(r_i^{(1)}) = \frac{4\bar{\theta}^2 r_i^{(1)2}}{l_0^2} - \frac{l_0^2}{4\bar{\theta}^2 r_i^{(1)2}} \quad (37)$$

at the lower boundary of the homogeneous layer, $r = r_i^{(1)}$. For the considered case this value is negative. The absolute value of σ_θ decreases until the interface between the layers is reached; at this point, the absolute value of σ_θ exhibits discontinuity. That follows by a rapid increase in the stress component in the anisotropic layer. At some point in the anisotropic layer, the sign of the stress changes and the stress becomes positive. This radius describes the neutral line, which is found to be in the anisotropic layer. The azimuthal stress component reaches the maximum at the upper boundary of the anisotropic layer, $r = r_i^{(2)} + h^{(2)}$.

As the lamination angle increases, we observe similar shapes and behaviour of the stress distribution functions; although the curves share some similarities, it is obvious that the absolute values of the stress components decrease with an increase in the lamination angle. We will analyse the role of the microstructure parameters in more detail next. In particular, we will focus on the elastic energy stored in the structure subjected to finite bending.

Figure 11 shows the dependence of the normalized energy density $\tilde{\Psi} = \hat{\Psi}/[\mu^{(m)}(h^{(1)} + h^{(2)})]$ on bending angle $\bar{\theta}$ for composites with different lamination angles ($\phi = \pi/36$ (a), $\pi/18$ (b), $\pi/12$ (c) and $\pi/9$ (d)). The results are presented for composites with various volume fractions of the stiffer phase in the anisotropic layer, namely, from $c^{(i)} = 0$ (dotted lower curve) to 1 (dashed upper curve) with a

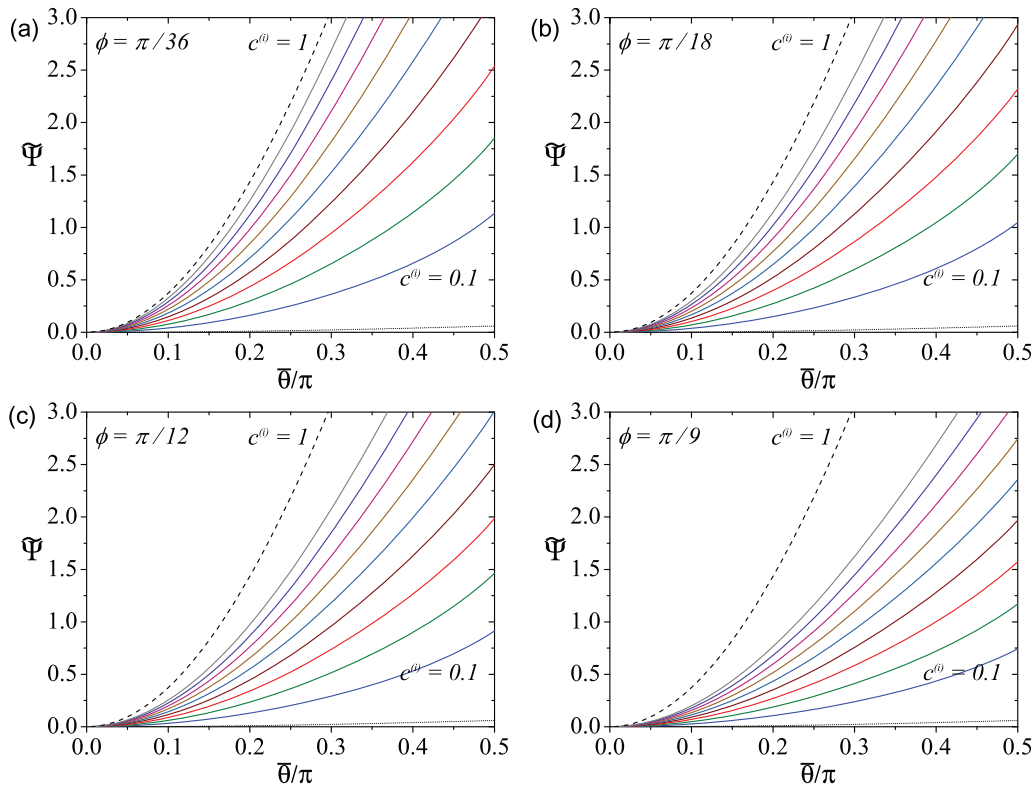


FIG. 11. Dependence of the energy density on the bending angle. The lamination angles are $\phi = 5^\circ$ (a), $\phi = 10^\circ$ (b), $\phi = 15^\circ$ (c) and $\phi = 20^\circ$ (d).

step of 0.1 from curve to curve. The geometrical length-to height ratio is $l_0/h = 5$, and the heights of anisotropic and isotropic layers are equal for all composites in Fig. 11.

Clearly, the stored energy increases as the loading is increased. The purely homogeneous material ($c^{(i)} = 0$) provides the lower bound for the energy, while the upper bound is provided by the response of the sandwich structure (soft lower and stiff upper homogeneous layers) that corresponds to $c^{(i)} = 1$. As expected, we observe that curves for composites with larger volume fraction of the stiff material approach the upper limit of $c^{(i)} = 1$. At small lamination angle, for example, $\phi = \pi/36$, there is a rather significant jump in the curves when the volume fraction of the stiffer phase is increased from $c^{(i)} = 0$ to $c^{(i)} = 0.1$; this is opposite to a less pronounced change in the curves from $c^{(i)} = 1$ to $c^{(i)} = 0.9$. The picture changes with an increase in the lamination angle. In particular, we observe that the energy density decreases with an increase in the lamination angle. Moreover, the drop at the upper limit ($c^{(i)} \rightarrow 1$) becomes more pronounced, while the jump at the lower limit ($c^{(i)} \rightarrow 0$) decreases.

Next we consider the influence of the lamination angle on the stored energy due to the finite bending of the structure. Figure 12 shows the dependence of the normalized stored energy on the lamination angle. The composites are subjected to $\bar{\theta} = 0.1\pi$ (a) and 0.5π (b). The results are presented for the same geometrical and microstructural parameters of the composites as for Fig. 11. The lower and upper bounds ($c^{(i)} = 0$ and $c^{(i)} = 1$, respectively) are denoted by thin dotted and dashed horizontal lines,

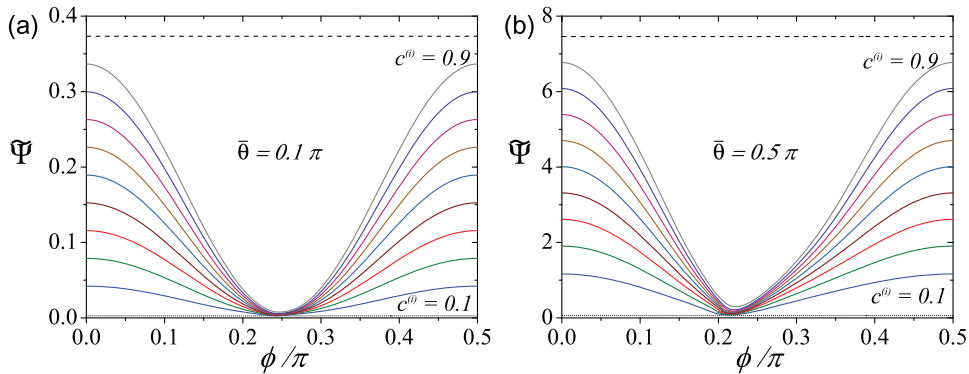


FIG. 12. Dependence of the energy density on the lamination angle. The structures are subjected to bending corresponding to $\bar{\theta} = \pi/10$ (a) and $\pi/2$ (b).

respectively. When inhomogeneity is present in the upper anisotropic layer, the curves take a non-linear shape with two local maxima at $\phi = 0$ and $\pi/2$, and one local minimum at about $\phi = \pi/4$, depending on the composite parameters and loading. Remarkably, in the vicinity of this local minimum, the composites are extremely flexible (for example the curve of $c^{(i)} = 0.9$). As the loading is increased (see Fig. 12(b) for $\bar{\theta} = 0.5\pi$), the local minima shift towards smaller lamination angles. The existence of the prominent minimum is of great importance and can be used for designing protective flexible materials with extreme properties.

5. Concluding remarks

We consider the mechanics of composite elasmoid fish scale assemblies and their bio-inspired analogues. We derive closed form analytical solutions for finite compression and bending. The analysis of these two fundamental modes of finite deformation reveals the role of the microstructure in the performance of the composites. For example, we reveal the existence of the super-flexible configurations of the composites, which are governed by the lamination angle, while still affording protection. These super-flexible composites can be manufactured with large volume fraction of the stiff phase, and hence, great protective properties can be achieved almost without compromising flexibility.

We investigated in detail the remarkable mechanism of coupling of compressive loadings and simple shear deformation. This mechanism can be utilized, for example, in personal armour to prevent deformation and subsequent damage of tissues and vital organs. As an alternative, this phenomenon can be used in designing a class of actuators that convert compressive loads to a more complicated motion. In this case, it is useful to know that, at some particular small lamination angles, giant shear deformations can be achieved even for relatively small compressive deformations. These remarkable results illustrate the detailed study of these structures. We hope that the derived solutions will be useful for designing new materials for various applications.

Funding

This research was supported by the U.S. Army Research Office through the MIT Institute for Soldier Nanotechnologies under contract W911NF-13-D-0001.

REFERENCES

- BROWNING, A., ORTIZ, C. & BOYCE, M. (2013) Mechanics of composite elasmoid fish scale assemblies and their bioinspired analogues. *J. Mech. Behav. Biomed. Mater.*, **19**, 75–86.
- BRUET, B., SONG, J., BOYCE, M. & ORTIZ, C. (2008) Materials design principles of ancient fish armour. *Nature Mater.*, **7**, 748–756.
- CONNORS, M., EHRLICH, H., HOG, M., GODEFFROY, C., ARAYA, S., KALLAI, I., GAZIT, D., BOYCE, M. & ORTIZ, C. (2012) Three-dimensional structure of the shell plate assembly of the chiton *tonicella marmorea* and its biomechanical consequences. *J. Struct. Biol.*, **177**, 314–328.
- DEBOTTON, G. (2005) Transversely isotropic sequentially laminated composites in finite elasticity. *J. Mech. Phys. Solids*, **53**, 1334–1361.
- DESTRADE, M., GILCHRIST, M. & MURPHY, J. (2010) Onset of nonlinearity in the elastic bending of blocks. *J. Appl. Mech., Trans. ASME*, **77**, 061015.
- DESTRADE, M., NÍ ANNAIDH, A. & COMAN, C. (2009) Bending instabilities of soft biological tissues. *Int. J. Solids Struct.*, **46**, 4322–4330.
- LI, Y., KAYNIA, N., RUDYKH, S. & BOYCE, M. C. (2013) Wrinkling of interfacial layers in stratified composites. *Adv. Eng. Mater.*, **15**, 921–926.
- MERODIO, J. & NEFF, P. (2006) A note on tensile instabilities and loss of ellipticity for a fiber-reinforced nonlinearly elastic solid. *Arch. Mech.*, **58**, 293–303.
- MERODIO, J. & OGDEN, R. W. (2002) Material instabilities in fiber-reinforced nonlinearly elastic solids under plane deformation. *Arch. Mech. (IPPT)*, **54**, 525–552.
- MERODIO, J. & OGDEN, R. (2005) Remarks on instabilities and ellipticity for a fiber-reinforced compressible nonlinearly elastic solid under plane deformation. *Quart. Appl. Math.*, **63**, 325–333.
- MEYERS, M., LIN, Y., OLEVSKY, E. & CHEN, P.-Y. (2012) Battle in the amazon: arapaima versus piranha. *Adv. Eng. Mater.*, **14**, B279–B288.
- NESTOROVIC, M. D. & TRIANTAFYLIDIS, N. (2004) Onset of failure in finitely strained layered composites subjected to combined normal and shear loading. *J. Mech. Phys. Solids*, **52**, 941–974.
- OGDEN, R. W. (1997) *Non-Linear Elastic Deformations*. New York: Dover Publications.
- OGDEN, R. W. (2008) Nonlinear elasticity and fibrous structure in arterial wall mechanics. *Lecture Notes for Summer School on Modeling and Computation in Biomechanics*. Austria: Graz University of Technology.
- RIVLIN, R. S. (1949) Large elastic deformations of isotropic materials. v. the problem of flexure. *Proc. R. Soc. A*, **195**, 463–473.
- ROCCABIANCA, S., BIGONI, D. & GEI, M. (2011) Long wavelength bifurcations and multiple neutral axes of elastic layered structures subject to finite bending. *J. Mech. Mat. Struct.*, **6**, 511–527.
- ROCCABIANCA, S., GEI, M. & BIGONI, D. (2010) Plane strain bifurcations of elastic layered structures subject to finite bending: theory versus experiments. *IMA J. Appl. Math.*, **75**, 525–548.
- RUDYKH, S. & BERTOLDI, K. (2013) Stability of anisotropic magnetorheological elastomers in finite deformations: a micromechanical approach. *J. Mech. Phys. Solids*, **61**, 949–967.
- RUDYKH, S., BHATTACHARYA, K. & DEBOTTON, G. (2014) Multiscale instabilities in soft heterogeneous dielectrics. *Proc. R. Soc. A*, **470**, 20130618.
- RUDYKH, S. & BOYCE, M. (2014a) Transforming small localized loading into large rotational motion in soft anisotropically-structured materials.
- RUDYKH, S. & BOYCE, M. (2014b) Transforming wave propagation in layered media via instability-induced interfacial wrinkling. *Phys. Rev. Lett.*, **112**, 034301.
- RUDYKH, S. & DEBOTTON, G. (2012) Instabilities of hyperelastic fiber composites: micromechanical versus numerical analyses. *J. Elasticity*, **106**, 123–147.
- SONG, J., REICHERT, S., KALLAI, I., GAZIT, D., WUND, M., BOYCE, M. & ORTIZ, C. (2010) Quantitative microstructural studies of the armor of the marine threespine stickleback (*gasterosteus aculeatus*). *J. Struct. Biol.*, **171**, 318–331.

- TRIANTAFYLIDIS, N. & MAKER, B. N. (1985) On the comparison between microscopic and macroscopic instability mechanisms in a class of fiber-reinforced composites. *J. Appl. Mech., Trans. ASME*, **52**, 794–800.
- YANG, W., CHEN, I. H., GLUDOVATZ, B., ZIMMERMANN, E. A., RITCHIE, R. O. & MEYERS, M. A. (2013) Natural flexible dermal armor. *Adv. Mater.*, **25**, 31–48.
- ZHU, D., ORTEGA, C., MOTAMEDI, R., SZEWCIW, L., VERNEREY, F. & BARTHELAT, F. (2012) Structure and mechanical performance of a ‘modern’ fish scale. *Adv. Eng. Mater.*, **14**, B185–B194.
- ZHU, D., SZEWCIW, L., VERNEREY, F. & BARTHELAT, F. (2013) Puncture resistance of the scaled skin from striped bass: Collective mechanisms and inspiration for new flexible armor designs. *J. Mech. Behav. Biomed. Mater.*, **24**, 30–40.